Acoustic-vortex generation through orbital angular momentum transfer

Rahim Amiri, Mahboubeh Mahdavi, and Mohammad Mahmoudi*
Department of Physics, University of Zanjan, University Boulevard, 45371-38791 Zanjan, Iran

(Received 5 September 2023; accepted 5 February 2024; published 20 February 2024)

We explore the phenomenon of orbital angular momentum (OAM) transfer within a high-quality single-crystal diamond mechanical resonator containing nitrogen-vacancy (NV) centers. By employing a weak acoustic field in conjunction with two microwave fields, we establish a three-level closed-loop system within the spin-triplet ground states 3*A* of the NV center. Analytical findings illuminate the potential for OAM transfer to take place, originating from Laguerre-Gaussian microwave fields and extending to the input acoustic field, consequently engendering an acoustic vortex. In this context, the initial weak microwave probe field is presumed to possess OAM content, and the transference of OAM to the input acoustic field is meticulously examined through the mechanism of three-wave mixing under the condition of multiphoton resonance. We extend our investigation to encompass a composite acoustic vortex, accounting for nonzero radial indices and topological charges attributed to both microwave fields. The outcomes of this paper bear significance as they hold the promise of refining the precision of acoustic sensors deployed in applications encompassing sonar systems, nondestructive testing, medical procedures, medical imaging, and synchronized acoustical tweezers.

DOI: 10.1103/PhysRevA.109.023523

I. INTRODUCTION

In recent years, there has been a growing acknowledgment of the transfer of two fundamental properties of light—spin and angular momentum—to matter, as demonstrated in various experiments [1,2]. The transfer of orbital angular momentum (OAM) from vortex beams to matter results in the generation of an azimuthal force at the object's center, causing the object to rotate in an orbit centered on the vortex core. These vortex beams, which carry OAM, exhibit a null pressure amplitude at the core and possess a spiral phase dislocation [3]. A screw dislocation exhibits a phase variation around its core represented by $e^{il\varphi}$, where φ denotes the azimuth angle, and l corresponds to the topological charge (also known as the azimuthal index) for various wave types, including optical waves [4], acoustic waves [5,6], and electron waves [7]. The screw wavefront of a vortex beam exhibits clockwise rotation for a positive topological charge and counterclockwise rotation for a negative topological charge. Several techniques have been developed for the detection and measurement of OAM in vortex electromagnetic beams [8,9]. The first ultrasonic beam with a helical phase wavefront was produced in 1998 by Hefner and Marston [3]. In recent years, significant attention has been devoted to the study of acoustic waves with spiral phases and OAM due to their diverse applications in various fields. These applications include nondestructive and contactless manipulation of microparticles [10,11], biomedical applications [12,13], and enhancing the capacity of acoustic communication [14,15].

An intriguing application of the acoustic vortex is found in acoustic tweezers, showcasing considerable potential as a technological advancement for trapping and manipulating microparticles or cells. This is achieved through the targeted implementation of a focused ultrasound beam, consequently obviating the need for direct physical contact [16]. In contrast to optical tweezers, which may induce deleterious photothermal damage through absorption-induced heating or photochemical damage via the excitation of reactive compounds like singlet oxygen, acoustic tweezers offer a more favorable approach to maintaining cell integrity. Additionally, acoustic tweezers demonstrate a distinct advantage in facilitating *in vivo* studies by enabling precise cell manipulation. In the context of acoustical tweezers, it is noteworthy that, for most particles of practical interest, objects with positive contrast factors, such as rigid particles or cells, are typically expelled from the focal point of a focused wave. Acoustical vortices present an elegant solution to this challenge, offering a mechanism to overcome such limitations and enhance the effectiveness of acoustic tweezers [12].

Due to their significant impact, numerous methods, based on active phase control consisting of a phased spiral source [17–19] or passive structure with a physically spiral source [20–24], have been proposed for the generation of acoustic vortices [25]. These techniques offer a variety of approaches for creating and manipulating acoustic vortices, enabling their application in various fields. It is essential to highlight that the use of active phased arrays is hindered by electronic complexity and high power consumption, limiting their practical application potential. Additionally, the spatial aliasing effect resulting from the bulky size of existing active elements reduces the effective areas of the generated spatial patterns and compromises the quality of the acoustic vortex, leading to decreased manipulation efficiency [26]. Analog apertures are also unsuitable due to their complexity, high cost, and the need for separate apertures to generate diverse acoustic-vortex

*mahmoudi@znu.ac.ir

modes. Therefore, it becomes highly intriguing and important to explore alternative and effective methods for the generation of acoustic vortices. Finding such methods could unlock new possibilities and applications for acoustic-vortex-based technologies. Nonlinear processes offer a highly efficient means for generating acoustic vortices across different frequencies, presenting a contrast to conventional approaches. Numerous theoretical contributions have been reported, aimed at describing the OAM exchange between electromagnetic fields [27–36]. These studies explore the potential transfer of OAM between different light frequencies. Notably, Juzeliūnas *et al.* [33,34] investigated the exchange of OAM modes using four- and five-level quantum systems. Furthermore, several other works have focused on the transfer of optical vortices, including those involving four-level electromagnetically induced transparency [27], coherent population trapping [28], and phaseonium media [29]. Recent research has demonstrated the exchange of optical vortices between different frequencies by leveraging interdot tunneling [37]. Moreover, the interaction of optical vortices with a crystal of four-level molecular magnets has been studied, revealing the occurrence of OAM transfer between different frequencies via the four-wave mixing mechanism in the microwave region [38]. These investigations collectively pave the way for new possibilities in the efficient generation and manipulation of acoustic vortices. It is noteworthy that considerable research has been conducted on vortex microwave and radio beams. However, the investigation into acoustic vortices has experienced a notable surge, particularly following the publication of two comprehensive review papers by Thomas *et al.* in 2017 [39] and Baudoin and Thomas in 2020 [40]. However, there is a notable gap in our understanding of acoustic-vortex generation and manipulation, making it an intriguing and promising area for future research.

Inspired by recent research, our paper focuses on the transfer of OAM in a high-Q single-crystal diamond mechanical resonator (DMR) embedded with nitrogen-vacancy (NV) centers from the microwave to the acoustic wave. The NV center in a diamond crystal consists of a nitrogen atom adjacent to a carbon vacancy in various orientations relative to N, making it a solid-state point defect. Due to its long electronic spin coherence time at room temperature [41,42], the NV center has found extensive applications in solid-state quantum physics experiments, quantum information processing [43,44], and magnetometry [45,46].

In the ground state, the NV center has a total spin angular momentum of $S = 1$, resulting in a spin-triplet ground state with different eigenvalues of S_z: $m_s = 0, +1, -1$. The corresponding states with $m_s = 0$ and ± 1 experience a zero-field splitting of approximately 2.87 GHz [47]. The application of an external magnetic field lifts the degeneracy and splits the states $|\pm 1\rangle$, allowing for the study of the NV center's quantum dynamics in the spin-triplet ground state. However, the coupling between the degenerate levels $|+1\rangle$ and $|-1\rangle$ is restricted. To overcome this limitation, we utilize the strain-mediated coupling mechanism in the DMR. The DMR is a diamond cantilever embedded with NV centers, enabling coupling between the energy levels of the NV center's ground state through the microwave and strain fields. The strain field is generated by lattice vibrations and transmitted into the DMR via a thin piezoelectric film grown on the surface of the diamond layer [47,48]. In other words, the electric strain induced can be effectively controlled by an external voltage.

With the notable optical capabilities of the diamond NV centers, numerous studies have explored coherent interactions between light and the NV centers, revealing intriguing optical phenomena. These studies include entanglement between photons and spins [49], entanglement among single spins [50], coherent population trapping [51], electromagnetically induced transparency [52], magneto-optical rotation [53], four-wave mixing [54], optical bistability [55], and magneto-optic dual switching [56]. Additionally, electromagnetically induced acoustic wave transparency (EIAT) [57] and phase control of EIAT [58] have been reported in high-Q single-crystal diamond nanomechanical resonators embedded with NV centers.

Based on the above-mentioned studies and the remarkable optical capabilities of diamond NV centers, our paper focuses on a sample of a diamond NV center interacting with a vortex beam. We investigate the exchange of optical vortices in a three-level closed-loop system of the NV center's ground state in the DMR, in the presence of a strain field and two microwave fields. Our findings reveal that a single probe beam carrying an OAM, initially shined on one transition of the spin states of the ground-state triplet of the NV center, creates an acoustic vortex with the same azimuthal and radial indices as that of the incident beam. It is noteworthy that the energy difference associated with the strain field transition in the NV center can be regulated by the static magnetic field. Consequently, the proposed technique can cover the generation of the acoustic vortices from a few kHz to the hypersonic GHz band. Moreover, we demonstrate that interference of two initially nonzero vortices generates a pattern of complex beams with peripheral vortices propagating inside a sample of a diamond NV center in the DMR. This paper provides valuable insights into the manipulation of optical vortices and acoustic vortices in a solid-state system, offering potential applications in quantum and optical technologies.

II. THEORETICAL FRAMEWORK

Consider the configuration of a closed-loop three-level system involving spin-triplet ground states ($3A$) within the NV center. This arrangement is depicted in Fig. 1. Among the levels, the state $|m_s = 0\rangle$ displays distinct characteristics due to spin-spin interactions, setting it apart from the other two states, $|m_s = \pm 1\rangle$. When a static magnetic field surpasses 102 mT, the state $|m_s = -1\rangle$ shifts below $|m_s = 0\rangle$ due to this interaction effect, as reported by Jin *et al.* [59].

In this setup, the system is subjected to a microwave field with a Rabi frequency denoted as $\Omega_c = \vec{\mu}_{23} \cdot \vec{E}_c/\hbar$, driving the transition between states $|2\rangle$ and $|3\rangle$. Simultaneously, another transition between states $|1\rangle$ and $|2\rangle$ is induced by a weak microwave field exhibiting Laguerre-Gaussian (LG) characteristics. The Rabi frequency for this latter field is represented as $\Omega_{\rm pr} = \vec{\mu}_{12} \cdot \vec{E}_{\rm pr}/\hbar$. Additionally, the typically forbidden transition $|1\rangle \leftrightarrow |3\rangle$ can be coherently excited by an acoustic field with a Rabi frequency $\lambda = \vec{\mu}_{13} \cdot \vec{E}_a/\hbar$, which can be generated using a thin piezoelectric device, as discussed by Ovartchaiyapong *et al.* [60]. Here, E_c, $E_{\rm pr}$, and E_a show the

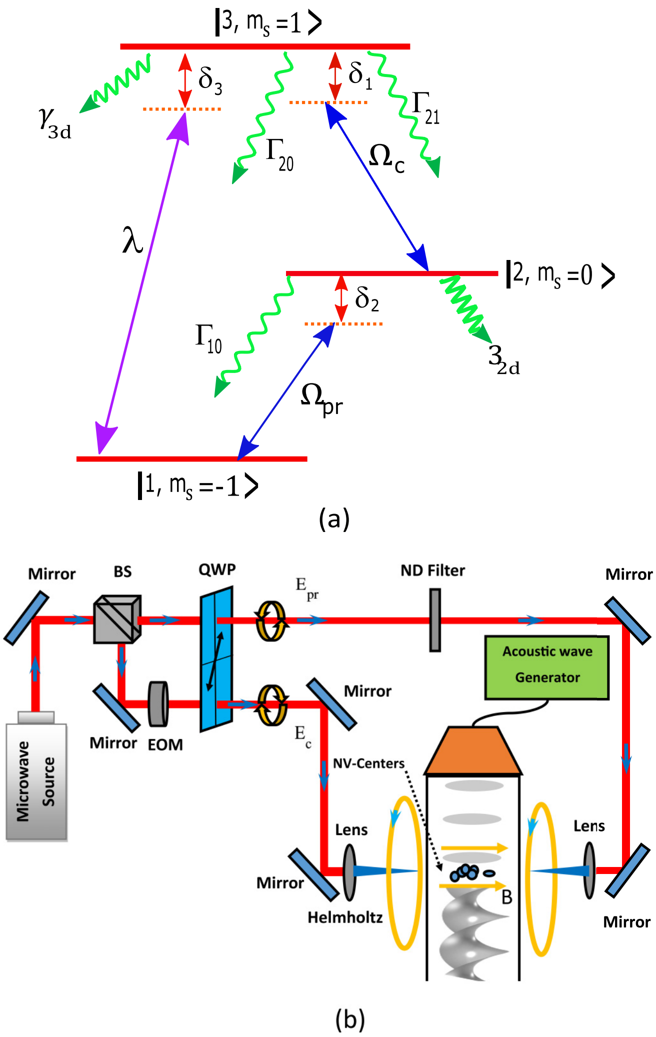

FIG. 1. (a) Schematic representation of the three-level closed-loop system within the ground-state configuration of the NV center. The transition $|1\rangle \leftrightarrow |3\rangle$ is excited by an acoustic wave field characterized by the Rabi frequency λ. Additionally, the transitions $|1\rangle \leftrightarrow |2\rangle$ and $|2\rangle \leftrightarrow |3\rangle$ are excited by two separate microwave fields possessing Rabi frequencies denoted as $\Omega_{\rm pr}$ and Ω_c, respectively. (b) The diagram illustrates the proposed experimental setup, where the electro-optical modulator, quarter-wave plate, neutral-density filter, and mirrors are represented by the abbreviations EOM, QWP, ND, and M, respectively.

amplitude of the coupling, probe, and acoustic fields, respectively. Moreover, $\vec{\mu}_{12}$, $\vec{\mu}_{23}$, and $\vec{\mu}_{13}$ are the electric dipole moments of the corresponding transitions.

The expression for the LG field in cylindrical coordinates is given by

$$E(r,\varphi) = E_0 \frac{1}{\sqrt{|l|!}} \left(\frac{\sqrt{2}r}{w_{\rm LG}}\right)^{|l|} L_p^{|l|}\left(\frac{2r^2}{w_{\rm LG}^2}\right) e^{-\frac{r^2}{w_{\rm LG}^2}} \times e^{i\left[\frac{n\omega}{c} z\left(1+\frac{r^2}{2(z^2+z_R^2)}\right)-(2p+|l|+1)\tan^{-1}\left(\frac{z}{z_R}\right)+l\varphi\right]}. \quad (1)$$

Here, E_0, $w_{\rm LG}$, n, ω, c, z, l, and p represent the strength, beam waist, refractive index of the medium, light frequency, velocity of light in vacuum, propagation direction of light, and azimuthal (OAM) and radial indices of the LG modes, respectively. Additionally, $z_R = n\omega w_{\rm LG}^2/2c$ stands for the Rayleigh range. The associated Laguerre polynomial, denoted as $L_p^{|l|}$, is expressed in the following form:

$$L_p^{|l|}(x) = \frac{e^x x^{-|l|}}{p!} \frac{d^p}{dx^p}[x^{|l|+p} e^{-x}], \quad (2)$$

where $x = 2r^2/w_{\rm LG}^2$ determines the radial dependence of the LG beams for different radial mode numbers.

The diagram depicting the proposed experimental configuration is illustrated in Fig. 1(b). A microwave source serves as the source for generating two microwave fields, one with left polarization (E_c) and the other with right polarization ($E_{\rm pr}$). The microwave beam traverses a polarized beam splitter, dividing the light into reflected S-polarized and transmitted P-polarized beams. Subsequently, each beam undergoes passage through a quarter-wavelength plate to establish left and right circular polarized microwave fields before being directed towards a diamond NV center. For manipulating the detunings, an electro-optical modulator can be employed. The intensity of each beam is adjustable via a neutral-density filter. External magnetic fields are applied to the diamond NV centers through the utilization of Helmholtz coils. The diamond NV center is poised to convert acoustic waves into an acoustic vortex, in the presence of the microwave and magnetic fields by means of OAM transfer.

Using the Liouville equation and multiphoton resonance condition, we derive the density matrix equation of motion for the three-level closed-loop system as follows:

$$\begin{aligned}
\dot{\rho}_{22} &= \Gamma_{31}\rho_{33} - \Gamma_{21}\rho_{22} - \gamma_{2d}\rho_{22} \\
&\quad + i\Omega_{\rm pr}\rho_{12} + i\Omega_c^* e^{-i\phi}\rho_{32} - i\Omega_{\rm pr}^*\rho_{21} - i\Omega_c e^{i\phi}\rho_{23}, \\
\dot{\rho}_{33} &= -\gamma_{3d}\rho_{33} - (\Gamma_{32} + \Gamma_{31})\rho_{33} \\
&\quad + i\lambda\rho_{13} + i\Omega_c e^{-i\phi}\rho_{23} - i\lambda^*\rho_{31} - i\Omega_c^*\rho_{32}, \\
\dot{\rho}_{12} &= \left[-i\delta_{\rm pr} - \frac{\Gamma_{21} + \gamma_{2d}}{2}\right]\rho_{12} \\
&\quad + i\Omega_{\rm pr}^*\rho_{22} + i\lambda^*\rho_{32} - i\Omega_{\rm pr}^*\rho_{11} - i\Omega_c e^{i\phi}\rho_{13}, \\
\dot{\rho}_{13} &= \left[-i\delta_\lambda - \frac{(\Gamma_{32} + \Gamma_{31}) + \gamma_{3d}}{2}\right]\rho_{13} \\
&\quad + i\lambda^*(\rho_{33} - \rho_{11}) + i\Omega_{\rm pr}^*\rho_{23} - i\Omega_c^* e^{-i\phi}\rho_{12}, \\
\dot{\rho}_{23} &= \left[-i\delta_c - \frac{\Gamma_{21} + \gamma_{2d}}{2} - \frac{(\Gamma_{32} + \Gamma_{31}) + \gamma_{3d}}{2}\right]\rho_{23} \\
&\quad + i\Omega_{\rm pr}\rho_{13} + i\Omega_c^* e^{-i\phi}(\rho_{33} - \rho_{22}) - i\lambda^*\rho_{21}, \\
\dot{\rho}_{11} &= -(\dot{\rho}_{22} + \dot{\rho}_{33}). \quad (3)
\end{aligned}$$

Here, Γ_{ij} is the spontaneous emission from $|i\rangle$ to $|j\rangle$ and $\gamma_{3d}(\gamma_{2d})$ is the dephasing rate of the state $|3\rangle(|3\rangle)$. The steady-state analytical expressions for the coherence terms, ρ_{21} and ρ_{31} by solving Eq. (3) for $\Gamma_{32} = \Gamma_{31} = \gamma_{3d} = \gamma_1$ and $\Gamma_{21} = \gamma_{2d} = \gamma_2$, under exact resonance condition $\delta_c = \delta_{\rm pr} = \delta_\lambda = 0$, and in weak probe field approximation, can be written as

$$\rho_{21} = \frac{(3i\gamma_1\Omega_{\rm pr} - 2\lambda\Omega_c)}{2|\Omega_c|^2 + 3\gamma_1\gamma_2},$$
$$\rho_{31} = \frac{2(i\gamma_2\lambda - \Omega_c\Omega_{\rm pr})}{2|\Omega_c|^2 + 3\gamma_1\gamma_2}. \quad (4)$$

To further analyze the system's behavior, we consider the Maxwell wave equations under the slowly varying envelope approximation, as given by

$$\frac{\partial\Omega_{\rm pr}(z)}{\partial z} = i\frac{\alpha\Gamma_{21}}{2L}\rho_{21},$$
$$\frac{\partial\lambda(z)}{\partial z} = i\frac{\alpha\Gamma_{31}}{2L}\rho_{31}. \quad (5)$$

The parameter L signifies the length of the atomic medium, and α quantifies the optical depth for both fields. By incorporating the expressions for coherence terms ρ_{21} and ρ_{31} [Eq. (4)] into the wave equations [Eq. (5)], and assuming, $\lambda(z=0) = \lambda(r,\varphi)$ and $\Omega_{\rm pr}(z=0) = \Omega_{\rm pr}(r,\varphi)$, we derive an expression for the Rabi frequency of the acoustic wave field, as shown in

$$\lambda(r,\varphi,z) = \frac{\lambda(r,\varphi)[i(2\gamma_2\Gamma_{31} - 3\gamma_1\Gamma_{21})(e^{A_+} - e^{A_-})}{2D} + \frac{D(e^{A_+} + e^{A_-})]}{2B} - \frac{\Omega_{\rm pr}(r,\varphi)[4\Gamma_{31}\Omega_c(e^{A_+} - e^{A_-})]}{2D}, \quad (6)$$

where A_+, A_-, D, and $\Omega_{\rm pr}(r,\varphi)$ are given as follows:

$$A_\pm = \frac{z\alpha(-3\gamma_1\Gamma_{21} - 2\gamma_2\Gamma_{31} \pm iD)}{4L(2|\Omega_c|^2 + 3\gamma_1\gamma_2)},$$
$$D = \sqrt{16\Gamma_{21}\Gamma_{31}\Omega_c^2 - (3\gamma_1\Gamma_{21} - 2\gamma_2\Gamma_{31})^2}, \quad (7)$$

$$\Omega_{\rm pr}(r,\varphi) = \Omega_{p_{r0}}\frac{1}{\sqrt{|l|!}}\left(\frac{\sqrt{2}r}{w_{\rm LG}}\right)^{|l|} L_p^{|l|}(2r^2/w_{\rm LG}^2) \times e^{-r^2/w_{\rm LG}^2}\, e^{il\varphi}. \quad (8)$$

Equation (6) takes into account direct medium response as well as the scattering of the microwave probe field into the acoustic field via $|1\rangle \to |2\rangle \to |3\rangle$ three-photon transition [62]. The latter process contributes significantly to the transfer of OAM to the acoustic field.

III. RESULTS AND DISCUSSIONS

The central objective of this research paper is to induce the creation of an acoustic vortex by harnessing OAM transfer from a relatively low-intensity microwave field in a high-quality single-crystal DMR containing NV centers. As indicated by Eq. (6), our anticipation is that the OAM inherent in the microwave field can be conveyed to the associated acoustic field, primarily facilitated by the second term within the equation. This implies that the acoustic field obtains a vortexlike pattern if the initial microwave field possesses a vortex beam configuration. In the context of the NV center

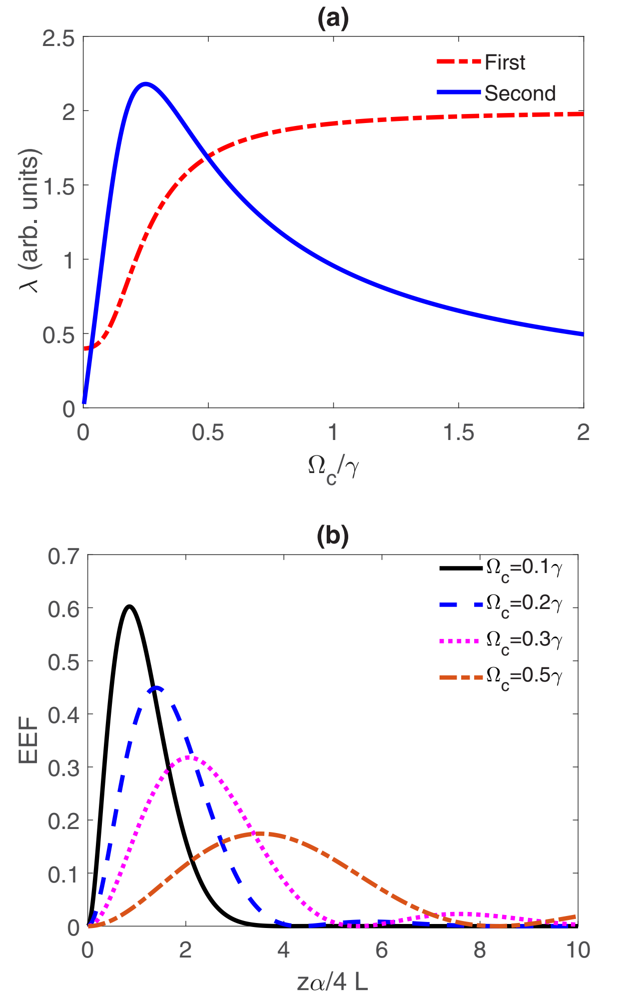

FIG. 2. The impact of the primary (dashed line) and secondary (solid line) components of the produced acoustic vortex in accordance with Eq. (6), as influenced by the coupling Rabi frequency. The employed parameter values are as follows: $\Gamma_{21} = 0.01\gamma$, $\Gamma_{31} = \gamma$, $\Gamma_1 = \gamma$, $\Gamma_2 = 0.01\gamma$.

in diamond, it is indeed possible to couple microwave and acoustic fields via magnetostrictive effect. The magnetostrictive effect refers to the change in dimensions of a material in response to an applied magnetic field [61]. In the case of NV centers, microwave radiation can be used to manipulate the electronic spin states of the NV center, leading to changes in the local magnetic field. These changes in the magnetic field, in turn, can induce mechanical vibrations (acoustic waves) in the diamond lattice through the magnetostrictive effect. However, to optimize the effectiveness of OAM transfer, it becomes imperative to minimize the impact of the first term. We achieve this by elevating the Rabi frequency associated with the coupling field. Through this adjustment, the prominence of the first term is magnified, leading to the facilitation of efficient OAM transfer even at relatively low values of the coupling Rabi frequency. In situations where $2|\Omega_c|^2 > 3\gamma_1\gamma_2$

holds true, we can reformulate Eq. (6) as follows:

$$\lambda(r,\varphi,z)=\frac{e^{-\frac{z\alpha}{4L}\frac{(2\gamma_2\Gamma_{31}+3\gamma_1\Gamma_{21})}{2|\Omega_c|^2}}}{D}\left\{\lambda(r,\varphi)\left[(3\gamma_1\Gamma_{21}-2\gamma_2\Gamma_{31})\right.\right.$$
$$\left.\times\sin\left(\frac{z\alpha}{4L}\frac{1}{\Omega_e}\right)+D\cos\left(\frac{z\alpha}{4L}\frac{1}{\Omega_e}\right)\right]$$
$$\left.-4i\Omega_{\mathrm{pr}}(r,\varphi)\Gamma_{31}\Omega_c\sin\left(\frac{z\alpha}{4L}\frac{1}{\Omega_e}\right)\right\}\qquad(9)$$

where $\Omega_e=\Omega_c/2\sqrt{\Gamma_{21}\Gamma_{31}}$. The graphical representation of the contributions stemming from both the first and second terms in Eq. (9) is depicted in Fig. 2(a), where they are plotted against the Rabi frequency of the coupling field. The utilized parameters consist of $\gamma_1=\gamma$, $\Gamma_{21}=0.01\gamma$, $\Gamma_{31}=\gamma$, and $\gamma_2=0.01\gamma$. Evidently, the contribution of the second term reaches its peak value at a specific coupling Rabi frequency, approximately determined by

$$\Omega_e=c_1\tan\left(\frac{z\alpha}{4L}\frac{1}{\Omega_e}\right)+\frac{c_2}{\Omega_e}\qquad(10)$$

where $c_1=(3\gamma_1\Gamma_{21}+2\gamma_2\Gamma_{31})/4\Gamma_{21}\Gamma_{31}$ and $c_2=3\gamma_1\gamma_2/4\Gamma_{21}\Gamma_{31}$. In this context, we explore a scenario wherein the vortex beam nature is attributed to the weak microwave field denoted as Ω_{pr}, while the acoustic field λ is approximated as a plane wave. All the outcomes presented in this paper are derived employing the formulation detailed in Eq. (6). Furthermore, the energy efficiency factor (EEF), denoted as the ratio of the square absolute value of the second term in Eq. (9) to the summation of the square absolute values of the applied Rabi frequencies, can be expressed as follows:

$$\mathrm{EEF}(z)=\frac{|\lambda(r,\varphi,z)|^2}{\Omega_{\mathrm{pr}}^2+\Omega_c^2}$$
$$=\left\{\frac{16\Omega_{\mathrm{pr}}^2\Omega_c^2\Gamma_{31}^2}{\Omega_{\mathrm{pr}}^2+\Omega_c^2}\frac{e^{-\frac{z\alpha}{2L}\frac{(2\gamma_2\Gamma_{31}+3\gamma_1\Gamma_{21})}{2|\Omega_c|^2}}}{|B|^2}\sin^2\left(\frac{z\alpha}{4L}\frac{1}{\Omega_e}\right)\right\}.\qquad(11)$$

Figure 2(b) depicts the relationship between the EEF and the dimensionless parameter $\frac{z\alpha}{4L}$ for a probe Rabi frequency $\Omega_{p_r}=0.03\gamma$ and varying coupling field strengths. The different curves are related to the different values of the coupling field, i.e., $\Omega_c=0.1\gamma$ (solid), 0.2γ (dashed), 0.3γ (dash-dotted), and 0.5γ (dotted). The parameters employed in Fig. 2(a) are consistent throughout. Analyzing Fig. 2(b) reveals that a higher EEF is evident at lower intensities of the coupling field. Nevertheless, the optimal coupling field strength can be determined by referring to the insights provided in Fig. 2(a) to achieve a high-quality output.

In Fig. 3, we illustrate the intensity (first row) and phase (second row) profiles of the resulting acoustic wave field corresponding to values of $\lambda=0.01\gamma_1$ [Fig. 3(a)] and $0.0001\gamma_1$ [Fig. 3(b)], with spatial dependencies on x and y at $z=L$. Various winding numbers $l\in-2,-1,\dots,2$ are considered, keeping the radial index fixed at $p=0$. The simulation parameters are set as follows: $\gamma_1=\gamma$, $\Gamma_{21}=0.01\gamma$, $\Gamma_{31}=\gamma$, $\gamma_2=0.01\gamma$, $w_{\mathrm{LG}}=0.5$ mm, $\Omega_{p_{r0}}=0.03\gamma_1$, and $\Omega_c=0.3\gamma_1$. The magnitude of the coupling Rabi frequency is judiciously chosen through Eq. (10) to minimize the influence of the first term in Eq. (9) on the transfer of OAM. The spatial axes x and y are scaled in millimeters. An inspection of Fig. 3 reveals that for $l=0$, the intensity profile assumes a Gaussian shape, with the highest intensity centered at $(x=0,y=0)$, while the phase profile remains constant across different x and y values. In the case of nonzero topological charges, the initial plane acoustic input field transforms into a vortex field, leading to doughnut-shaped intensity profiles featuring a central dark (blue) hollow region. Furthermore, discernible helical phase fronts emerge for nonzero l values, offering insight into the singularity present in the generated acoustic vortex. A comparison between Figs. 3(a) and 3(b) demonstrates that when dealing with a weak input acoustic field, the OAM of the weak probe field is faithfully transferred to the resulting acoustic field. Upon increasing the Rabi frequency of the input acoustic field, the intensity and phase profiles of the output acoustic field undergo slight adjustments in relation to the input weak probe field profile. This phenomenon arises from the fact that the generated acoustic vortex stems from a composite response of the medium, comprising both direct and indirect contributions, as articulated in Eq. (6). The indirect response, manifesting as the dominant second term in Eq. (6), primarily governs the OAM transfer. Conversely, the direct response exerts a mitigating influence, necessitating a reduction in the Rabi frequency of the weak input acoustic field to minimize its impact. Notably, the phase difference of the generated acoustic vortex with respect to the input weak LG microwave field is $\pi/2$, an outcome attributed to the coefficient $-i$ present in the second term of Eq. (9). Presently, our focus shifts toward the exploration of OAM transference involving higher LG modes within the framework of a feeble microwave field. Our objective is to induce the emergence of higher-order acoustic-vortex modes characterized by nonzero radial indices. Consequently, we consider a scenario where the weak probe field encompasses a nonzero radial index along with a distinct topological charge. Illustrated in Fig. 4, the ensuing acoustic vortex manifests itself through intensity representations (first row) and corresponding phase profiles (second row) for the specific configuration of $p=1$, encompassing a range of topological charges denoted by $l\in-2,-1,\dots,2$. The parameters adopted for this paper remain consistent with those employed in Fig. 3(b). It is notable that the intensity patterns featured in Fig. 4 exhibit dual concentric rings with a central region of darkness. This distinctive arrangement directly corresponds to the selected radial index $p=1$. The connection between the topological charge and the number of complete 2π phase cycles in the phase profile is well established. Consequently, the helical phase profile experiences an inversion as the sign of l changes. The findings delineated in Fig. 4 unequivocally demonstrate the successful transfer of OAM, leading to the generation of an acoustic vortex possessing a radial index of $p=1$ across a diverse set of topological charges spanning $l\in-2,-1,\dots,2$. Now, we delve into the influence wielded by the intensity profile of the initial feeble acoustic field on the emergence of an acoustic vortex. Our investigation unfolds with the adoption of a Gaussian-shaped profile for the weak input acoustic field. Within this context, we consider the inclusion of OAM

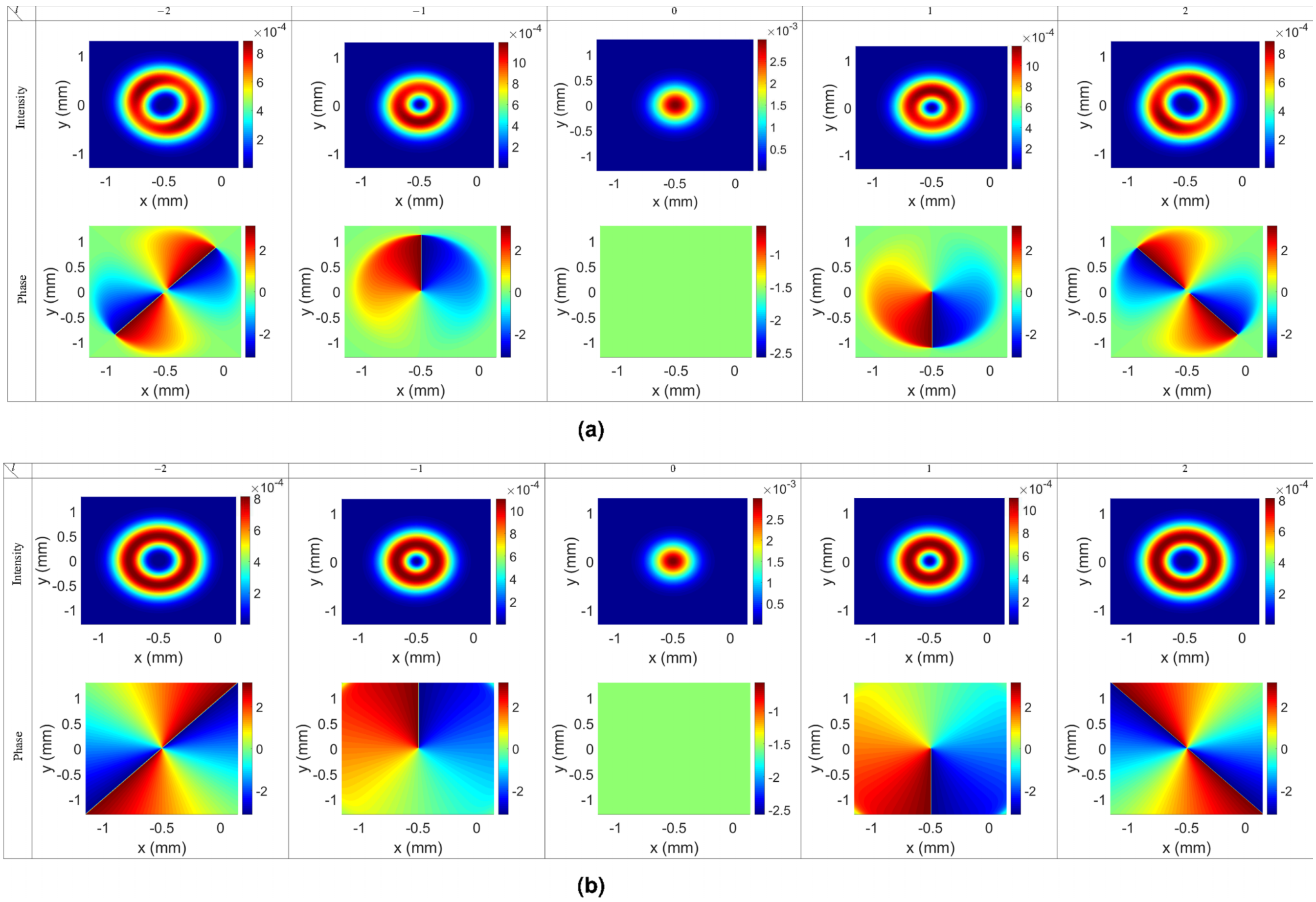

FIG. 3. Intensity (top row) and helical phase (bottom row) distributions of the generated acoustic vortex as functions of x and y, featuring a radial index of zero, for Rabi frequencies $\lambda = 0.01\gamma_1$ (a) and $0.0001\gamma_1$ (b). These profiles are presented for various winding numbers l_2 spanning from -2 to 2, with the observations taken at a distance of $z = L$. The following parameters are utilized: $w_{\mathrm{LG}} = 0.5$ mm, $\gamma_1 = \gamma$, $\Omega_{p_{r0}} = 0.03\gamma$, $\Omega_c = 0.3\gamma$, $\Gamma_{10} = 0.01\gamma$, $\Gamma_{20} = \gamma$, $\gamma_2 = 0.01\gamma$.

within the weak microwave probe field and scrutinize the consequent OAM transference. The outcomes, presented as intensity representations (first row) and corresponding phase profiles (second row) in Fig. 5, unveil the acoustic vortex's properties as functions of x and y for varying modes of the probe microwave field. Specifically, the exploration encompasses $l \in -2, -1, \ldots, 2$ for two cases: $p = 0$ [Fig. 4(a)] and $p = 1$ [Fig. 4(b)]. The parameters utilized for these investigations mirror those detailed in Fig. 3(b). Upon close examination of the findings in Fig. 5, it is evident that the effective transfer of OAM to the weak input acoustic field is proficiently achieved across both zero and nonzero

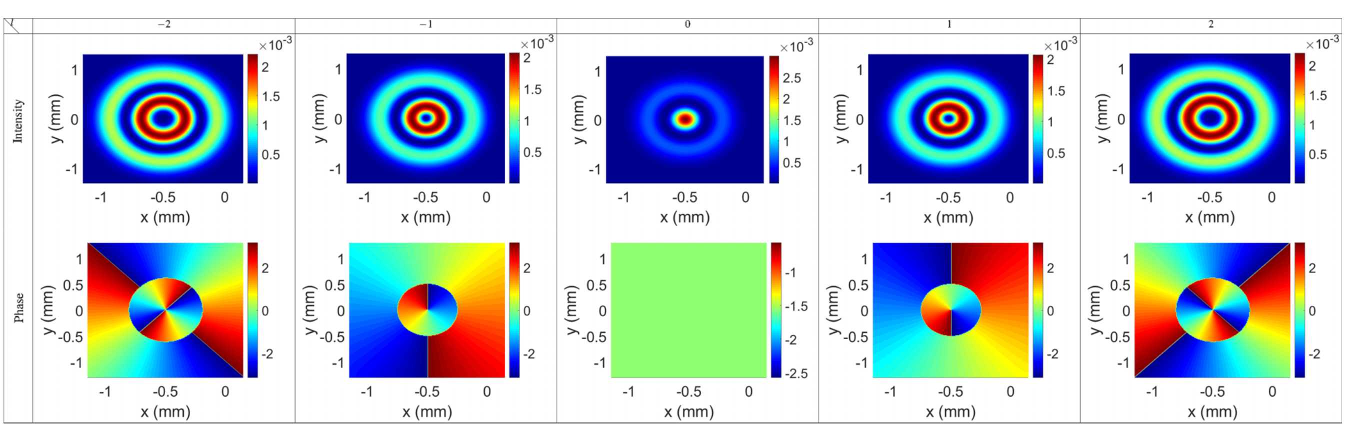

FIG. 4. Intensity (top row) and helical phase distribution (bottom row) of the generated acoustic vortex, depicted as functions of spatial coordinates x and y, corresponding to $p = 1$ and winding numbers $l \in -2, -1, \ldots, 2$, under the influence of a weak probe field. The parameter values are consistent with those detailed in Fig. 3(b).

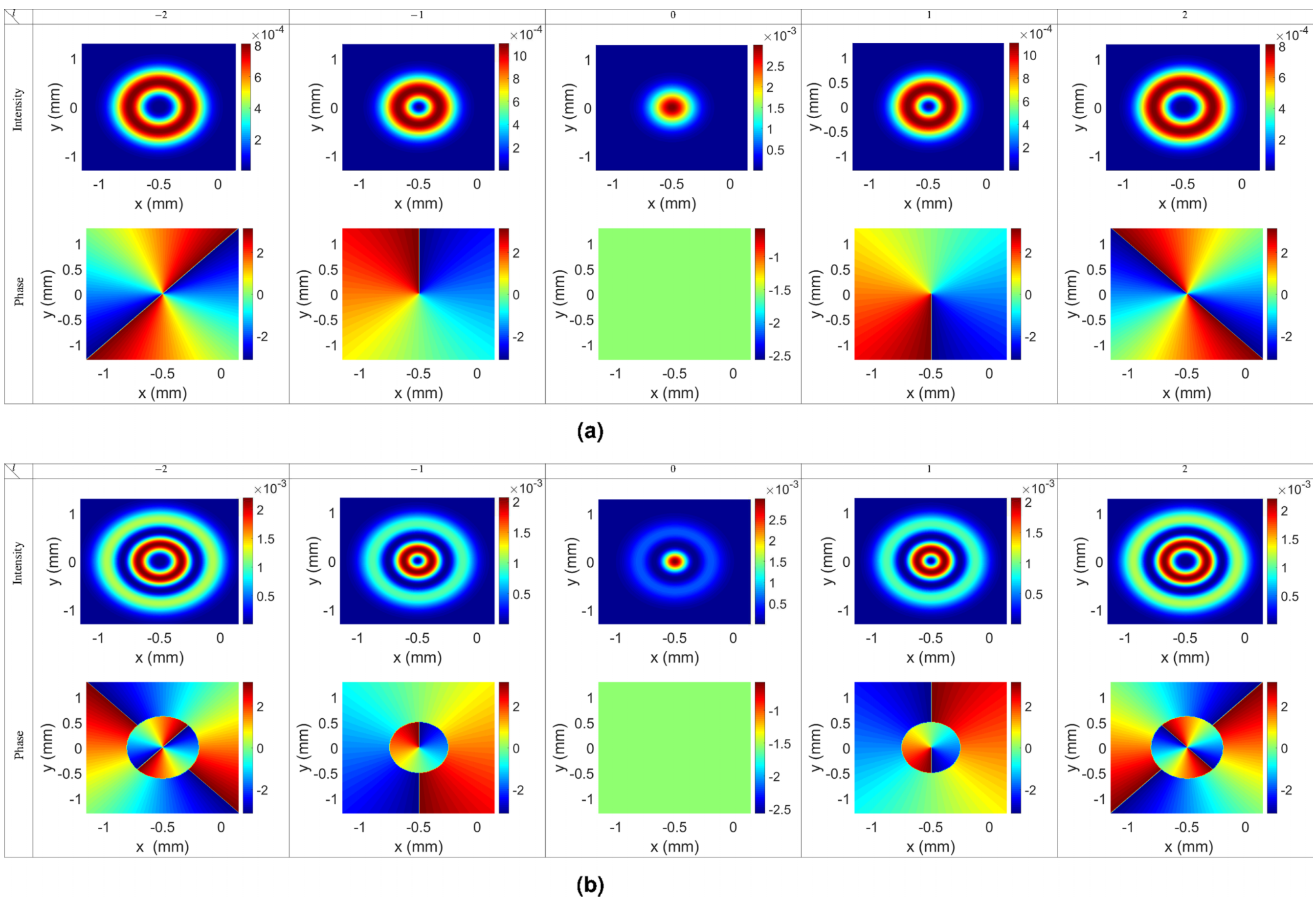

FIG. 5. Intensity profile (top row) and phase distribution (bottom row) of the generated acoustic vortex as functions of spatial coordinates x and y, for different modes of the weak probe field with $l \in -2, -1, \ldots, 2$ for $p = 0$ (a) and $p = 1$ (b). The input weak acoustic field is characterized by a Gaussian-shaped profile. The parameter values remain consistent with those elucidated in Fig. 3(b).

radial indices in the context of the planar input weak acoustic field.

Lastly, our attention turns to the generation of a composite acoustic vortex employing LG microwave fields. This intricate scenario envisions both the coupling and the weak probe fields to possess OAM attributes, prompting an in-depth inquiry into OAM transference to the input acoustic field. It is anticipated that this composite setup engenders the transfer of a blend of diverse modes. Figure 6 offers a visual representation of the intensity [Fig. 6(a)] and the helical phase [Fig. 6(b)] profiles associated with varying topological charges. The employed configuration involves LG-profiled probe and coupling fields characterized by zero radial indices and diverse topological charges. The parameters align with those enlisted in Fig. 3(b). The outcomes underscore that the generated acoustic vortex embodies a cumulative topological charge given by $l_{\rm pr} + l_c$, orchestrated through a three-wave mixing mechanism encompassing the $|1\rangle \rightarrow |2\rangle \rightarrow |3\rangle \rightarrow |1\rangle$ transitions. This results in an amalgamation of OAM attributes. Notably, a distinct scenario emerges when probe and coupling fields adopt opposing OAM attributes, manifesting as a doughnut-shaped intensity profile devoid of any vortex features, emblematic of zero OAM. However, the scenario takes on a distinct character when both the probe and coupling fields embrace nonzero radial indices. In this configuration, the generated acoustic vortex emerges as a linear superposition of various modes [37]. Figure 7 articulates this phenomenon, portraying the intensity (first row) and helical phase (second row) profiles of the composite acoustic vortex across diverse topological charges and radial indices. The corresponding linear superposition terms are indicated atop each profile. Notably, each linear superposition term incorporates LG modes with a cumulative topological charge of $l_{\rm pr} + l_c$ and radial indices p_c, $p_{\rm pr}$, and $p_c + p_{\rm pr}$. This arises from the interference of two or more vortex beams and proves valuable for the accurate manipulation of two distinct microparticles and human cells using synchronized acoustical tweezers [63].

IV. CONCLUDING REMARKS

We have presented a straightforward theoretical approach for acoustic-vortex generation in a high-Q single-crystal DMR embedded with NV centers via OAM transfer. Our paper reveals that the OAM associated with a low-intensity microwave field can be effectively transmitted to an acoustic field, thereby instigating the emergence of an acoustic vortex through the mechanism of three-wave mixing. The composite acoustic vortex has been theoretically generated when two microwave-

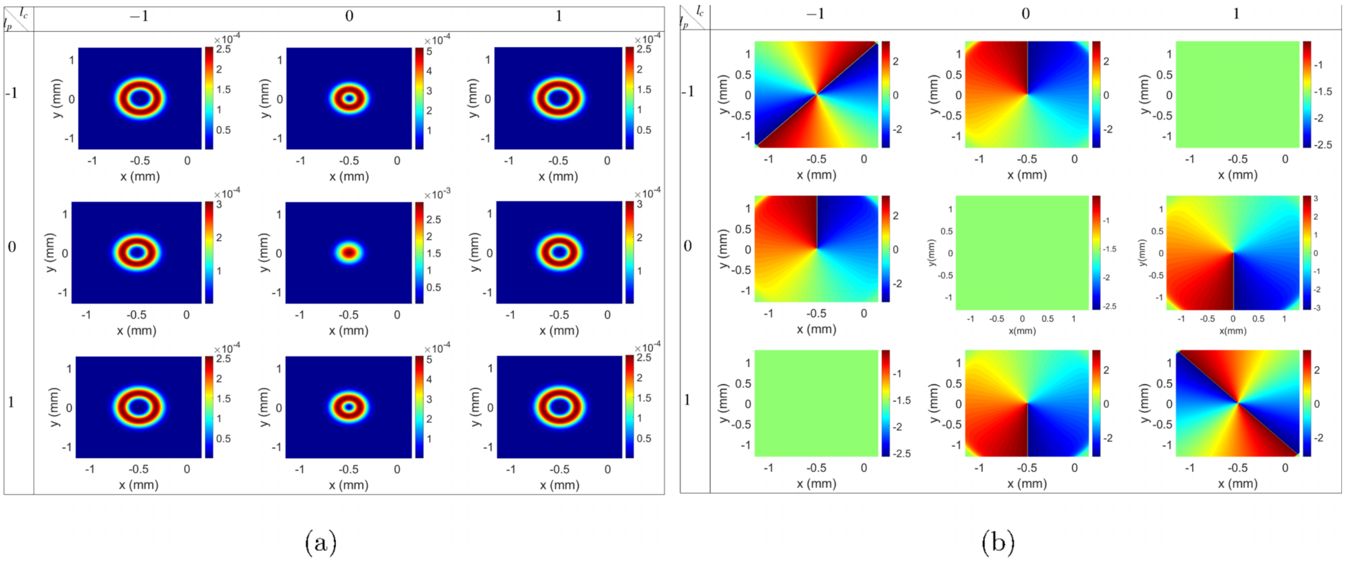

FIG. 6. Intensity (a) and helical phase (b) distributions of the produced acoustic vortex, presented as functions of spatial coordinates x and y. The probe and coupling fields exhibit LG profiles characterized by a zero radial index, and they encompass diverse topological charges. The remaining parameters are consistent with those detailed in Fig. 3(b).

applied fields contain OAM. This paper lays the foundation for potential applications in manipulating acoustic fields using OAM-based techniques.

ACKNOWLEDGMENTS

We would like to express our deepest appreciation to Dr. H. R. Hamedi for useful discussion.

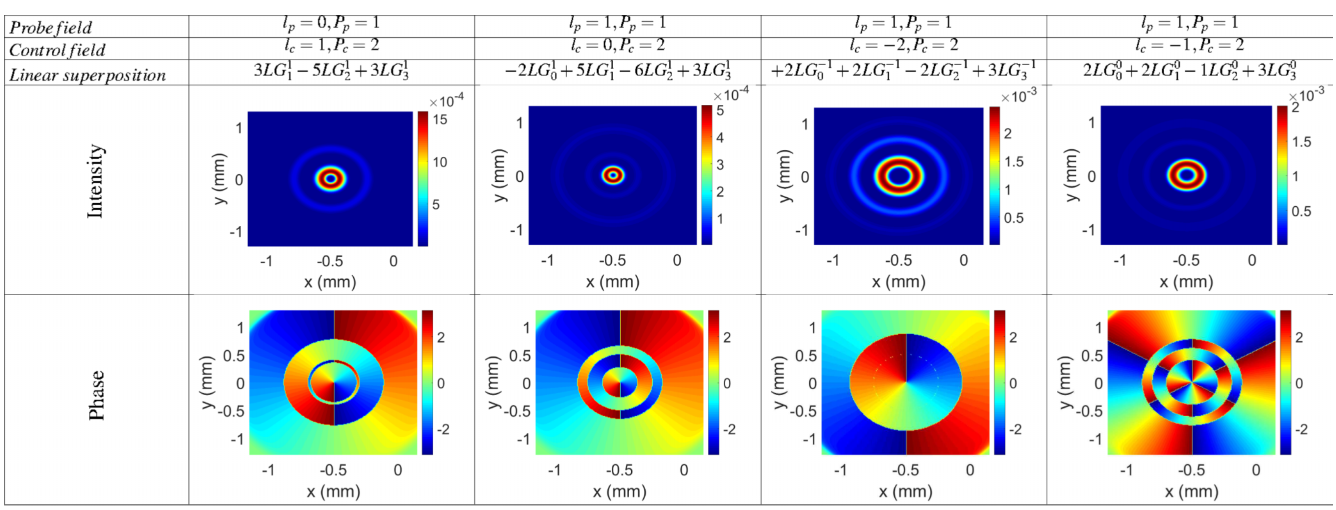

FIG. 7. Intensity (first row) and helical phase (second row) distributions of the composite acoustic vortex, presented as functions of spatial coordinates x and y. The profiles correspond to various topological charges and radial indices for the probe and coupling fields. The superposition of the individual modes contributing to each profile is depicted above. The parameters utilized are consistent with those presented in Fig. 3(b).

[1] H. He, M. E. J. Friese, N. R. Heckenberg, and H. Rubinsztein-Dunlop, Direct observation of transfer of angular momentum to absorptive particles from a laser beam with a phase singularity, Phys. Rev. Lett. **75**, 826 (1995).

[2] N. B. Simpson, K. Dholakia, L. Allen, and M. J. Padgett, Mechanical equivalence of spin and orbital angular momentum of light: An optical spanner, Opt. Lett. **22**, 52 (1997).

[3] B. T. Hefner and P. L. Marston, Acoustical helicoidal waves and Laguerre-Gaussian beams: Applications to scattering and to angular momentum transport, J. Acoust. Soc. Am. **103**, 2971 (1998).

[4] L. Allen, M. W. Beijersbergen, R. J. C. Spreeuw, and J. P. Woerdman, Orbital angular momentum of light and the transformation of Laguerre-Gaussian laser modes, Phys. Rev. A **45**, 8185 (1992).

[5] B. T. Hefner and P. L. Marston, An acoustical helicoidal wave transducer with applications for the alignment of ultrasonic and underwater systems, J. Acoust. Soc. Am. **106**, 3313 (1999).

[6] L. Zhang and P. L. Marston, Angular momentum flux of nonparaxial acoustic vortex beams and torques on axisymmetric objects, Phys. Rev. E **84**, 065601(R) (2011).

[7] M. Uchida and A. Tonomura, Generation of electron beams carrying orbital angular momentum, Nature (London) **464**, 737 (2010).

[8] Z. Zhang, J. Pei, Y. P. Wang, and X. Wang, Measuring orbital angular momentum of vortex beams in optomechanics, Front. Phys. **16**, 32503 (2021).

[9] S. Hamideh Kazemi and M. Mahmoudi, Identifying orbital angular momentum of light in quantum wells, Laser Phys. Lett. **16**, 076001 (2019).

[10] A. Marzo, S. A. Seah, B. W. Drinkwater, D. R. Sahoo, B. Long, and S. Subramanian, Holographic acoustic elements for manipulation of levitated objects, Nat. Commun. **6**, 8661 (2015).

[11] A. Marzo, M. Caleap, and B. W. Drinkwater, Acoustic virtual vortices with tunable orbital angular momentum for trapping of Mie particles, Phys. Rev. Lett. **120**, 044301 (2018).

[12] M. Baudoin, J. L. Thomas, R. A. Sahely, J. C. Gerbedoen, Z. Gong, A. Sivery, O. B. Matar, N. Smagin, P. Favreau, and A. Vlandas, Spatially selective manipulation of cells with single-beam acoustical tweezers, Nat. Commun. **11**, 4244 (2020).

[13] Z. Gong and M. Baudoin, Three-dimensional trapping and dynamic axial manipulation with frequency-tuned spiraling acoustical tweezers: A theoretical study, Phys. Rev. Appl. **16**, 024034 (2021).

[14] X. Jiang, B. Liang, J.-C. Cheng, and C.-W. Qiu, Twisted acoustics: Metasurface enabled multiplexing and demultiplexing, Adv. Mater. **30**, 1800257 (2018).

[15] C. Shi, M. Dubois, Y. Wang, and X. Zhang, High-speed acoustic communication by multiplexing orbital angular momentum, Proc. Natl. Acad. Sci. USA **114**, 7250 (2017).

[16] J. Yoo, J. Kim, J. Lee, and H. H. Kim, Red blood cell trapping using single-beam acoustic tweezers in the Rayleigh regime, iScience **26**, 108178 (2023).

[17] A. Marzo and B. W. Drinkwater, Holographic acoustic tweezers, Proc. Natl. Acad. Sci. USA **116**, 84 (2019).

[18] R. D. Muelas-Hurtado, J. L. Ealo, J. F. Pazos-Ospina, and K. Volke-Sepúlveda, Generation of multiple vortex beam by means of active diffraction gratings, Appl. Phys. Lett. **112**, 084101 (2018).

[19] M. Baudoin, J.-C. Gerbedoen, A. Riaud, O. B. Matar, N. Smagin, and J.-L. Thomas, Folding a focalized acoustical vortex on a flat holographic transducer: Miniaturized selective acoustical tweezers, Sci. Adv. **5**, eaav1967 (2019).

[20] C. Liu, H. Long, C. Ma, Y. Jia, C. Shao, Y. Cheng, and X. Liu, Broadband acoustic vortex beam generator based on coupled resonances, Appl. Phys. Lett. **118**, 143503 (2021).

[21] Y. Jin, R. Kumar, O. Poncelet, O. Mondain-Monval, and T. Brunet, Flat acoustics with soft gradient-index metasurfaces, Nat. Commun. **10**, 143 (2019).

[22] H. Zhou, J. Li, K. Guo, and Z. Guo, Generation of acoustic vortex beams with designed Fermat's spiral diffraction grating, J. Acoust. Soc. Am. **146**, 4237 (2019).

[23] X. Jiang, Y. Li, B. Liang, J.-C. Cheng, and L. Zhang, Convert acoustic resonances to orbital angular momentum, Phys. Rev. Lett. **117**, 034301 (2016).

[24] H. Esfahlani, L. Herve, and J. R. Mosig, Generation of acoustic helical wavefronts using metasurfaces, Phys. Rev. B **95**, 024312 (2017).

[25] S. Guo, Z. Ya, P. Wu, and M. Wan, A review on acoustic vortices: Generation, characterization, applications and perspectives, J. Appl. Phys. **132**, 210701 (2022).

[26] C. R. P. Courtney, B. W. Drinkwater, C. E. M. Demore, S. Cochran, A. Grinenko, and P. D. Wilcox, Dexterous manipulation of microparticles using Bessel-function acoustic pressure fields, Appl. Phys. Lett. **102**, 123508 (2013).

[27] H. R. Hamedi, J. Ruseckas, and G. Juzeliūnas, Exchange of optical vortices using an electromagnetically-induced-transparency based four-wave-mixing setup, Phys. Rev. A **98**, 013840 (2018).

[28] H. R. Hamedi, E. Paspalakis, G. Žlabys, G. Juzeliūnas, and J. Ruseckas, Complete energy conversion between light beams carrying orbital angular momentum using coherent population trapping for a coherently driven double-Λ atom-light-coupling scheme, Phys. Rev. A **100**, 023811 (2019).

[29] H. R. Hamedi, J. Ruseckas, E. Paspalakis, and G. Juzeliūnas, Transfer of optical vortices in coherently prepared media, Phys. Rev. A **99**, 033812 (2019).

[30] H. R. Hamedi, J. Ruseckas, E. Paspalakis, and G. Juzeliūnas, Off-axis optical vortices using double-Raman singlet and doublet light-matter schemes, Phys. Rev. A **101**, 063828 (2020).

[31] Y. Hong, Z. Wang, D. Ding, and B. Yu, Ultraslow vortex four-wave mixing via multiphoton quantum interference, Opt. Express **27**, 29863 (2019).

[32] J. Qiu, Z. Wang, D. Ding, W. Li, and B. Yu, Highly efficient vortex four-wave mixing in asymmetric semiconductor quantum wells, Opt. Express **28**, 2975 (2020).

[33] J. Ruseckas, A. Mekys, and G. Juzeliūnas, Slow polaritons with orbital angular momentum in atomic gases, Phys. Rev. A **83**, 023812 (2011).

[34] J. Ruseckas, V. Kudriašov, A. Y. Ite, and G. Juzeliūnas, Transfer of orbital angular momentum of light using two-component slow light, Phys. Rev. A **87**, 053840 (2013).

[35] Z. Amini Sabegh, M. A. Maleki, and M. Mahmoudi, Microwave-induced orbital angular momentum transfer, Sci. Rep. **9**, 3519 (2019).

[36] Z. A. Sabegh, M. Mohammadi, M. A. Maleki, and M. Mahmoudi, Orbital angular momentum transfer via spontaneously generated coherence, J. Opt. Soc. Am. B **36**, 2757 (2019).

[37] M. Mahdavi, Z. Amini Sabegh, M. Mohammadi, M. Mahmoudi, and H. R. Hamedi, Manipulation and exchange of light with orbital angular momentum in quantum-dot molecules, Phys. Rev. A **101**, 063811 (2020).

[38] M. Mahdavi, Z. Amini Sabegh, H. R. Hamedi, and M. Mahmoudi, Orbital angular momentum transfer in molecular magnets, Phys. Rev. B **104**, 094432 (2021).

[39] J. L. Thomas, R. Marchiano, and D. Baresch, Acoustical and optical radiation pressure and the development of single beam

acoustical tweezers, J. Quant. Spectrosc. Radiat. Transfer **195**, 55 (2017).

[40] M. Baudoin and J.-L. Thomas, Acoustic tweezers for particle and fluid micromanipulation, Annu. Rev. Fluid Mech. **52**, 205 (2020).

[41] P. L. Stanwix, L. M. Pham, J. R. Maze, D. Le Sage, T. K. Yeung, P. Cappellaro, P. R. Hemmer, A. Yacoby, M. D. Lukin, and R. L. Walsworth, Coherence of nitrogen-vacancy electronic spin ensembles in diamond, Phys. Rev. B **82**, 201201(R) (2010).

[42] T. A. Kennedy, J. S. Colton, J. E. Butler, R. C. Linares, and P. J. Doering, Long coherence times at 300 K for nitrogen-vacancy center spins in diamond grown by chemical vapor deposition, Appl. Phys. Lett. **83**, 4190 (2003).

[43] M. V. G. Dutt, L. Childress, L. Jiang, E. Togan, J. Maze, F. Jelezko, A. S. Zibrov, P. R. Hemmer, and M. D. Lukin, Quantum register based on individual electronic and nuclear spin qubits in diamond, Science **316**, 1312 (2007).

[44] J. Wrachtrup and F. Jelezko, Processing quantum information in diamond, J. Phys.: Condens. Matter **18**, S807 (2006).

[45] J. R. Maze, P. L. Stanwix, J. S. Hodges, S. Hong, J. M. Taylor, P. Cappellaro, L. Jiang, M. V. Gurudev Dutt, E. Togan, A. S. Zibrov, A. Yacoby, R. L. Walsworth, and M. D. Lukin, Nanoscale magnetic sensing with an individual electronic spin in diamond, Nature (London) **455**, 644 (2008).

[46] G. Balasubramanian, I. Y. Chan, R. Kolesov, M. Al-Hmoud, J. Tisler, C. Shin, C. Kim, A. Wojcik, P. R. Hemmer, A. Krueger, T. Hanke, A. Leitenstorfer, R. Bratschitsch, F. Jelezko, and J. Wrachtrup, Nanoscale imaging magnetometry with diamond spins under ambient conditions, Nature (London) **455**, 648 (2008).

[47] M. W. Doherty, F. Dolde, H. Fedder, F. Jelezko, J. Wrachtrup, N. B. Manson, and L. C. L. Hollenberg, Theory of the ground-state spin of the NV^-center in diamond, Phys. Rev. B **85**, 205203 (2012).

[48] J. R. Maze, A. Gali, E. Togan, Y. Chu, A. Trifonov, E. Kaxiras, and M. D. Lukin, Properties of nitrogen-vacancy centers in diamond: The group theoretic approach, New J. Phys. **13**, 025025 (2011).

[49] E. Togan, Y. Chu, A. S. Trifonov, L. Jiang, J. Maze, L. Childress, M. V. G. Dutt, A. S. Sørensen, P. R. Hemmer, A. S. Zibrov, and M. D. Lukin, Quantum entanglement between an optical photon and a solid-state spin qubit, Nature (London) **466**, 730 (2010).

[50] P. Neumann, N. Mizuochi, F. Rempp, P. Hemmer, H. Watanabe, S. Yamasaki, V. Jacques, T. Gaebel, F. Jelezko, and J. Wrachtrup, Multipartite entanglement among single spins in diamond, Science **320**, 1326 (2008).

[51] C. Santori, P. Tamarat, P. Neumann, J. Wrachtrup, D. Fattal, R. G. Beausoleil, J. Rabeau, P. Olivero, A. D. Greentree, S. Prawer, F. Jelezko, and P. Hemmer, Coherent population trapping of single spins in diamond under optical excitation, Phys. Rev. Lett. **97**, 247401 (2006).

[52] V. M. Acosta, K. Jensen, C. Santori, D. Budker, and R. G. Beausoleil, Electromagnetically induced transparency in a diamond spin ensemble enables all-optical electromagnetic field sensing, Phys. Rev. Lett. **110**, 213605 (2013).

[53] A. Mortezapour, M. Ghaderi Goran Abad, and M. Ahmadi Borji, Magneto-optical rotation in the diamond nitrogen-vacancy center, Laser Phys. Lett. **13**, 055202 (2016).

[54] J. Li, R. Yu, C. Ding, and Y. Wu, Optical bistability and four-wave mixing with a single nitrogen-vacancy center coupled to a photonic crystal nanocavity in the weak-coupling regime, Opt. Express **22**, 15024 (2014).

[55] D. Zhang, R. Yu, J. Li, C. Ding, and X. Yang, Laser-polarization-dependent and magnetically controlled optical bistability in diamond nitrogen-vacancy centers, Phys. Lett. A **377**, 2621 (2013).

[56] J.-H. Li, R. Yu, and Y. Wu, Propagation of magnetically controllable lasers and magneto-optic dual switching using nitrogen-vacancy centers in diamond, J. Appl. Phys. **113**, 103104 (2013).

[57] Q. Hou, W. Yang, C. Chen, and Z. Yin, Electromagnetically induced acoustic wave transparency in a diamond mechanical resonator, J. Opt. Soc. Am. B **33**, 2242 (2016).

[58] S. Evangelou, Phase control of electromagnetically induced acoustic wave transparency in a diamond nanomechanical resonator, Phys. Lett. A **381**, 1624 (2017).

[59] L. Jin, M. Pfender, N. Aslam, P. Neumann, S. Yang, J. Wrachtrup, and R.-B. Liu, Proposal for a room-temperature diamond maser, Nat. Commun. **6**, 8251 (2015).

[60] P. Ovartchaiyapong, K. W. Lee, B. A. Myers, and A. C. B. Jayich, Dynamic strain-mediated coupling of a single diamond spin to a mechanical resonator, Nat. Commun. **5**, 4429 (2014).

[61] E. W. Lee, Magnetostriction and magnetomechanical effects, Rep. Prog. Phys. **18**, 184 (1955).

[62] M. Mahmoudi and J. Evers, Light propagation through closed-loop atomic media beyond the multiphoton resonance condition, Phys. Rev. A **74**, 063827 (2006).

[63] Z. Gong and M. Baudoin, Particle assembly with synchronized acoustic tweezers, Phys. Rev. Appl. **12**, 024045 (2019).